Molecular Frame Reconstruction using Time-domain Photoionization Interferometry Supplementary Material

Claude Marceau,[1] Varun Makhija,[2] Dominique Platzer,[1] A. Yu. Naumov,[1] P. B. Corkum,[1] Albert Stolow,[2,3,4] D. M. Villeneuve,[1] and Paul Hockett[4,*]

[1] *Joint Attosecond Science Laboratory, National Research Council of Canada and University of Ottawa, 100 Sussex Drive, Ottawa, K1A 0R6, Canada*
[2] *Department of Physics. University of Ottawa, 150 Louis Pasteur, Ottawa, ON K1N 6N5, Canada*
[3] *Department of Chemistry, University of Ottawa, 10 Marie Curies, Ottawa, ON K1N 6N6, Canada*
[4] *National Research Council of Canada, 100 Sussex Drive, Ottawa, K1A 0R6, Canada*

In this document additional theory and results are presented, providing supplementary details and discussion to the brief report provided in the main manuscript. Associated data and code is available online at https://dx.doi.org/10.6084/m9.figshare.4480349.

I. PHOTOIONIZATION MODEL

In the main text, a simplified formalism for the full angular interferograms, or photoelectron angular distributions (PADs), resulting from an aligned molecular ensemble, as defined by the $\beta_{L,M}(t)$ parameters, is provided, viz.:

$$\beta_{L,M}(t) = \sum_{K,Q} \left(\sum_{\alpha,\alpha'} \gamma_{K,Q}^{\alpha,\alpha'} \boldsymbol{D}_{\alpha}^{*} \boldsymbol{D}_{\alpha'} \right) A_{K,-Q}(t) \tag{1}$$

In this formalism, as noted in the manuscript: all of the angular momentum coupling terms are denoted by γ, and can be defined analytically; $A_{K,-Q}(t)$ are the ADMs, and $\boldsymbol{D}_{\alpha}$ the symmetrized ionization matrix elements to be determined. All other required quantum numbers are denoted α, and the coherent summation is obtained by summing over all possible pairs of each quantum number.

The full formalism for the $\beta_{L,M}(t)$, following Underwood and Reid [1, 2], can be given as:

$$\begin{aligned}
\beta_{L,M}(t) = {} & (2L+1)^{1/2} \sum_{P} (-1)^{P} \begin{pmatrix} 1 & 1 & P \\ p & -p & R \end{pmatrix} e_{-p} e_{-p}^{*} \\
& \text{x} \sum_{K} \sum_{Q} (2K+1)^{1/2} \begin{pmatrix} P & K & L \\ Q-M & -Q & M \end{pmatrix} A_{K,-Q}(t) \\
& \text{x} \sum_{q,q'} (-1)^{q'} \begin{pmatrix} 1 & 1 & P \\ q & -q' & q'-q \end{pmatrix} \begin{pmatrix} P & K & L \\ q-q' & q'-q & 0 \end{pmatrix} \\
& \text{x} \sum_{l,l'} \sum_{\lambda,\lambda'} (-1)^{\lambda'} (2l+1)^{1/2} (2l'+1)^{1/2} \begin{pmatrix} l & l' & L \\ \lambda & -\lambda' & M \end{pmatrix} \begin{pmatrix} l & l' & L \\ 0 & 0 & 0 \end{pmatrix} \\
& \text{x} \; (-i)^{l'-l} \sum_{\Gamma,\Gamma'} \sum_{\mu,\mu'} \sum_{h,h'} b_{hl\lambda}^{\Gamma\mu *} b_{h'l'\lambda'}^{\Gamma'\mu'} \boldsymbol{D}_{hl}^{\Gamma\mu *}(q) \boldsymbol{D}_{h'l'}^{\Gamma'\mu'}(q')
\end{aligned} \tag{2}$$

In this form, as compared to the simplified form of eqn. 1, all terms subsumed into $\gamma_{K,Q}^{\alpha,\alpha'}$ are written in full, as are the set of required quantum numbers α, and the summations over all possible pairs of quantum numbers denoted by; the matrix elements $\boldsymbol{D}_{\alpha}$ are written as $\boldsymbol{D}_{hl}^{\Gamma\mu}(q)$. This formalism is also given in ref. [3], along with extended discussion - the text below is reproduced here for reference, with additions in parentheses:

> "The first line of equation 2 describes the polarization state of the ionizing radiation; the photon carries 1 unit of angular momentum with projection p onto the lab frame z-axis. For linearly polarized light aligned with the laboratory frame z-axis $p = 0$, hence from the 3-j symbol $P = 0,\, 2$ and $R = 0$. The spherical tensor components e_{-p} describe the polarization and amplitude of the ionizing radiation, for the case of linearly polarized light along the z-axis $e_{-p} = e_0 = e_z$ and the term $e_z e_z^{*}$ can be set to equal unity.
>
> The second & third lines of equation 2 describe the convolution of the molecular frame with the aligned axis distribution, $P(\theta, t)$, expressed as ADMs. The light field has molecular frame (MF) projection terms

q. Terms in $q = 0$ thus represent ionizing light polarized along the MF axis, while $q = \pm 1$ terms represent light polarized perpendicular to the MF axis. If the LF and MF are coincident then a single value of $q = p$ is selected, while an arbitrary rotation serves to mix terms in q as the LF polarization axis is projected onto different MF axes. This mixing (and averaging), due to the ADMs, is described by the coupling of P and K into the final multipole moments L.

The remaining lines of equation 2 deal with the photoelectron and "molecular" terms. Here (l, λ) represent the photoelectron partial wave components [4, 5], with (orbital) angular momentum l, and MF projection λ. The terms $\boldsymbol{D}_{hl}^{\Gamma\mu*}(q)$ represent the symmetrized radial components, with symmetrization coefficients $b_{hl\lambda}^{\Gamma\mu}$, of the (radial) dipole matrix elements for each symmetry-allowed continuum Γ [an irreducible representation (IR) of the scattering system point-group [6]] [2, 7, 8],

$$\boldsymbol{D}_{hl}^{\Gamma\mu}(q) = \langle \Psi_+;\, \psi_{hl,\,e}^{\Gamma\mu} | \sum_s r_s Y_{1q}(\hat{\mathbf{r}}_s) | \psi_i \rangle \tag{3}$$

where the summation is over all electrons s. [Additionally, μ is the degeneracy index, and h an additional index for states with the same (l, μ), see e.g. ref. [6, 9]] These matrix elements are complex, and may also be written in the form $\boldsymbol{D}_{hl}^{\Gamma\mu} = |\boldsymbol{D}_{hl}^{\Gamma\mu}| e^{-i\eta_{hl}^{\Gamma\mu}}$, where η is the total phase of the matrix element, often called the scattering phase. The radial matrix elements and phases are the only part of equation 2 which are not analytic functions and, in general, must be determined numerically [10, 11] or from experiment [12–14] for quantitative understanding of a given system. Symmetry-based arguments can, however, provide a means of determining which integrals are non-zero, hence which (l, λ) can appear in ψ_e. Such considerations therefore allow for phenomenological, qualitative, or possibly semi-quantitative, treatments of photoionization for a given molecule.

The effect of the averaging over a distribution of molecular axis directions is to lose sensitivity in the PADs. In particular, the observed anisotropy in the LFPAD cannot be more than that arising from the coupling of the probe photon to the aligned distribution of molecules, as can be seen from the 3-j term linking terms P, K, L. This limits L to the range $|P - K| ... P + K$ in integer steps. For instance, if the alignment is prepared by a single pump photon then a $\cos^2\theta$ axis distribution is created, and the only non-zero alignment parameters are $A_{0,0}$ and $A_{2,0}$. Because $P = 0, 2$ only, the alignment in this case would restrict $\beta_{LM}(t)$ to terms with $L = 0, 2, 4$ (additionally, for cylindrically symmetric cases, $M = -Q = 0$). As the degree of alignment increases higher-order $\cos^K(\theta)$ terms are required to describe the axis distribution and the LF ensemble result approaches the true MF [1]. Higher order terms in equation 2 can be observed, hence more information is present in the LFPAD and a greater sensitivity to any property which affects the PADs, e.g. the evolution of the axis distribution itself, intermediate state dynamics in a pump-probe experiment, and so on, may be obtained."

In this notation, the molecular frame (MF) result is given as [1, 2]:

$$\begin{aligned}
\beta_{L,M} = {} & (2L+1)^{1/2} \sum_P (-1)^P \begin{pmatrix} 1 & 1 & P \\ p & -p & R \end{pmatrix} e_{-p} e_{-p}^* \\
& \text{x} \sum_{q,q'} (-1)^{q'} \begin{pmatrix} 1 & 1 & P \\ q & -q' & q'-q \end{pmatrix} D^P_{(q-q'),R}(\phi,\theta,\chi) \\
& \text{x} \sum_{l,l'} \sum_{\lambda,\lambda'} (-1)^{\lambda'} (2l+1)^{1/2} (2l'+1)^{1/2} \begin{pmatrix} l & l' & L \\ \lambda & -\lambda' & M \end{pmatrix} \begin{pmatrix} l & l' & L \\ 0 & 0 & 0 \end{pmatrix} \\
& \text{x} \; (-i)^{l'-l} \sum_{\Gamma,\Gamma'} \sum_{\mu,\mu'} \sum_{h,h'} b_{hl\lambda}^{\Gamma\mu*} b_{h'l'\lambda'}^{\Gamma'\mu'} \boldsymbol{D}_{hl}^{\Gamma\mu*}(q) \boldsymbol{D}_{h'l'}^{\Gamma'\mu'}(q')
\end{aligned} \tag{4}$$

In this case, most terms are identical to the LF result, but in the MF only a single polarization geometry is defined, and terms related to the axis distribution $A_{K,-Q}(t)$ are not present. Instead, the second line of equation 4 describes the rotation of the polarization vector into the molecular frame with the rotation matrix element $D^P_{(q-q'),R}$, which rotates the multipole P with projection term R in the LF into the MF with projection $q - q'$ by rotation through the Euler angles (ϕ, θ, χ). In the MF, the geometric interferences resulting from different polarization geometries (i.e. different molecular axis orientations) are not present, hence the rotational wavepacket does not play a role and there is no time-dependence.

II. LIMITATIONS & GENERALIZATIONS

A. Theoretical limitations

In common with energy-domain complete experiments, the sign of the phases remains ambiguous for a cylindrically symmetric geometry, and additional measurements which break the symmetry [7, 15], or provide additional kinetic energy points [16] are required for disambiguation; alternatively, comparison with theory can be used to determine missing channel relations [16–18]. The use of rotational wavepackets does, however, allow access to interferences between different continua (q), which are not usually present in state-resolved measurements, thus the relative phase between components in different continua is defined.

For heteronuclear symmetric tops, similar considerations apply - orientational information, i.e. up-down asymmetries, which correspond to interferences between odd and even l, are generally inaccessible in cylindrically symmetric geometries. Again, symmetry breaking (via, e.g., polarization geometry) or additional information from theory can provide the additional information required. Aspects of this have been explored for the bench-mark case of NO, with the use of circularly polarized light [7, 15] and the determination of missing phases via theory [18]. Odd-even l interferences via ionizing transitions of different photon order has also been explored for control [19, 20].

Most generally, for asymmetric tops, some additional terms are present in eqn. 2 (see ref. [2]); similarly, the rotational wavepacket contains higher-dimensional moments ($Q \neq 0$ and $S \neq 0$, see ref. [2]). In this case, additional interferences are present, and the sign of the phases and odd-even l interferences, should be retrievable in principle, although may in practice be restricted by symmetry in specific cases. Orientational information (up-down asymmetries, corresponding to interferences between odd and even l) should also be observable, although further work remains to fully investigate the details in this case [21].

Finally, it is of note that the use of full time-series data making use of a rotational wavepacket, can be considered (as herein) as essentially a 'post-processing' approach, in which one assumes that the experimental data contains the necessary information content. In this case, the experiments may be regarded as general. Conversely, a 'pre-processing' approach can also be taken, in which one seeks to tailor the rotational wavepacket (or other experimentally-controllable geometric aspects, such as polarization geometry and the breaking of cylindrical symmetry) for specific channels or cases. In general, one might assume that a combination of these approaches will prove most successful: as indicated in the preceding discussion, additional measurements may be required in order to obtain a certain level of completeness in the retrieved matrix elements; for cases with high complexity, e.g. many matrix elements, high degrees of degeneracy, etc., or cases with relatively isotropic ionization dynamics, additional measurements may be required even for basic matrix element determination. Again, related discussion and application of these concepts to specific cases can be found in the existing literature, e.g. [7, 15–18, 22, 23].

B. Additional approximations

In the analysis presented herein, the ionization matrix elements are assumed to be constant over the energy range spanned by each photoelectron band. This is implicit in the bootstrapping methodology implemented, which made use of the data (sets of $\beta_{LM}(t)$) extracted from the measurements for each observed photoelectron band. In this case, as described in the main text, each band corresponds to a final electronic state. Essentially, this means that the retrieved matrix elements are averaged over any underlying structures or dynamics, depending on both the photoionization physics, the molecular properties and experimental time-scales involved. In general, for the ultrafast case in which the sudden approximation holds, and starting from a system in a vibronically cold initial state (i.e. relatively localised in coordinate space), it may be expected that this approximation is reasonable. Further detailed discussion on these points - and possible reasons for a breakdown of these approximations - can be found in, e.g., ref. [3] (sect. 2.4 and references therein), refs. [2, 24–26] for pump-probe type experiments, and ref. [8] for general discussion of the photoionization dynamics. For N_2, the expected range of variation of the matrix elements as a function of energy over a 1 eV range can be found in the ePolyScat results (Sec. VII), which indicate small but insignificant changes in the MFPADs over 1 eV ranges over the bands of interest; see also ref. [27] for an exploration of the variation of the matrix elements in vibrationally averaged cases, and ref. [28] which investigated multi-channel coupling effects theoretically, and suggests that these types of effects (resulting in sharp resonant features as a function of energy) may be seen clearly near threshold (< 5 eV).

C. Experimental considerations

Experimentally, the bandwidths of the high harmonic pulses were approx. 0.1 eV (H5@23.3 eV) and 0.16 eV (H7@32.6 eV), as measured using a time-of-flight spectrometer. The VMI instrument resolution under the experimental focussing conditions was estimated to be 0.13 eV (@4.5 eV) and 0.18 eV (@7.5 eV). Under these conditions vibrational bands could just be discerned in some measurements, but full vibrational resolution was not pursued further in these experiments, and (as noted above) the photoionization matrix elements were assumed to be invariant to the final energy and vibrational state over each band (or, at least, the retrieved results are final-state averaged). The good agreement of the retrieved MFPADs (for the X and A-channels) with the ePolyScat results, indicate that any final vibrational state and kinetic energy averaging does not have a significant effect on the analysis in this case (again, see Sec. VII for data discussion).

Generally, to investigate any underlying band-structure within the rotational wavepacket pump-probe methodology, one could potentially design/tune experiments to resolve features within each electronic band, by optimising spectrometer conditions (VMI has a trade-off between dynamic range and resolution, see e.g. [14, 29, 30]) and/or utilising narrower-bandwidth (i.e. longer) pulses, although this tuning is non-trivial for harmonic sources. There may be other means of exploring changes in the PAD over the pulse bandwidth, e.g. shifting the central frequency of the light, or deliberately preparing a vibrational wavepacket to investigate specific regions of the nuclear coordinate space [31, 32].

III. BOOTSTRAPPING METHODOLOGY

As discussed in the main text, we use herein a "bootstrapping" fitting approach, comprised of multiple steps which allow for separation of the two sets of unknowns, and a way to gradually bootstrap to the complete MF results via stages of analysis of increasing complexity. The nature of the fitting at each stage also provides a flexible methodology which can be used to carefully sample the solution hyperspace in order to ensure unique results, and fit with variable information content (experimental measurements) based on computational time and desired precision [33]. In all cases, the underlying physics provides stringent limits on the form of the fitting functions, hence the fitting procedure at each stage is expected to be somewhat reliable by construction. Further analysis of the results, including comparison with experimental parameters, additional data not used in the analysis, and *ab initio* calculations all provide additional means of cross-checking and verifying the extracted physical parameters.

In terms of information content, this bootstrapping procedure gradually increases both the experimental information content - the number of geometric configurations of the photoionization interferometer - and the level of physical information included (hence fitted/extracted) in the analysis. In the first step, ADMs are determined without the need for accurate treatment of the ionization probe [34]; in the second step this information is used as part of the calculation to determine the ionization dynamics. In the sub-steps to determine the ionization dynamics, the experimental information content included in the analysis is gradually increased: the initial coarse steps in this procedure provide a base-line high information content without the necessity for many temporal points via the selection of highly distinct molecular axis distributions, while latter sub-steps allow for fine-tuning of the data by gradually coupling additional time-steps into the analysis.

For the determination of the ionization dynamics, based on eqn. 2, multiple fits (approx. 100 independent fits for each channel) with relatively low convergence criteria, and randomised seed values, were performed for a small sub-set of the data around the alignment and anti-alignment features, making use of 11 experimental measurements (e.g. Fig. 1(b), points marked 'x'). This allowed for a rapid search of the solution hyperspace (of dimensions given by the number of fit parameters), and a means to check for the presence of multiple solution sets and local minima (see ref. [33] for further details and discussion). Secondly, the best parameter set(s), were used to seed fits with tighter convergence criteria. Thirdly, these results were tested against larger sub-sets of the data (Fig. 1, dashed lines), as an independent check for physical consistency, then fine-tuned via fitting to these larger sub-sets if required (Fig. 1(a)).

In this case, the 11 sets of $\beta_{L,M}(t)$ used in the initial step of the analysis allowed for a relatively rapid fitting procedure, taking around 30 minutes per fit in this case, using Matlab's (R2015b) LSQCURVEFIT function, which implements a Levenberg-Marquandt non-linear fitting routine, and running on a desktop machine based around a quad-core Intel Core i5-750CPU. Coupling additional sets of data into the fitting procedure scaled the time required, and there is naturally a balancing of computational time with accuracy, up to the point where the dataset is found to be sufficient to uniquely determine the desired physical parameters. In this case, best fit parameters from the initial minimal fitting were eventually fine-tuned with 89 distinct experimental datasets (with fits requiring many hours to run).

For the fitting, the partial wave expansion was truncated at $l_{max} = 5$. In the data, $L_{max} = 6$ is observed, suggesting that the lesser of K_{max} or l_{max}=3; based on this observation, and the fact that $K_{max} = 6$ from the linear fitting stage,

this cut-off was assumed sufficient. Additionally, this cut-off is consistent with the *ab initio* results (ePolyScat) results, which indicated that terms for $l > 5$ are negligible, with normalised magnitudes on the order of 10^{-5} or smaller.

Finally, it is also of note that the initial testing of the non-linear part of this analysis methodology was performed using "synthetic" results. In this case, test sets of (arbitrary) matrix elements were used to generate synthetic aligned-frame results (using a calculated rotational wavepacket), which were then analysed with the bootstrapping procedure (as per the experimental results). In the test cases, a few sets of matrix elements were trialled, corresponding to different cases (symmetry, relative magnitudes and phases). In all cases tested matrix element retrieval was reliable, which indicates that there are no symmetry or l-dependent bugs/errors in the analysis code, and provides further confidence that the experimentally retrieved results are reliable.

IV. FULL TIME-SERIES DATA AND FIT RESULTS

Figure 1 extends the presentation of the data and fit results shown in fig. 3 of the main article. In this case, all three channels are shown, along with the full $\beta_{L,M}(t)$ experimental data and fit results. Note that these results show full $\beta_{L,M}(t)$ values, normalized for a spherical harmonic expansion as given in eqn. 1 of the main article; this is distinct from the results shown in fig. 2 of the main article, which are normalized $\beta_L(t)$ values, corresponding to an expansion in Legendre polynomials.

As discussed in the main text, the wealth of data, and the high information content of $S(\theta, t)$, is clear. In this dataset, the X-channel is particularly sensitive to the axis distribution, with significant changes in both the yields and angular distributions, while the A-channel is much less sensitive and shows less dramatic variations in $S(\theta, t)$.

For the X-channel, two unique fit results (sets of matrix elements $\boldsymbol{D}_\alpha$) were obtained via statistical sampling at a coarse level (11 temporal points over the revival features, 100 independent, randomly seeded fits), and then fine-tuned via the bootstrapping methodology. In this case, additional temporal points (distinct sets of ADMs) were gradually incorporated into the fitting, thereby increasing the information content of the fitting, until there was no significant change in χ^2. At each stage, the fitting was seeded by the previous best results, thereby fine-tuning the previously determined matrix elements. This procedure eventually incorporated 89 temporal points, and led to a single best-fit solution (6 complex-valued matrix elements, results as shown in fig. 1(a)). The full set of matrix elements determined (inc. associated uncertainties) are given in the following section (table I).

For the A and B-channels the data becomes increasingly noisy as the yields decrease, and also indicates much less dramatic changes with the axis distribution. In these cases adequate fits were obtained at the coarse level (as indicated in fig. 1(b) & (c)), and further bootstrapping was not explored in either case. For the A-channel three best fit parameter sets were obtained (7 matrix elements), differing only in the perpendicular continuum waves. For the B-channel data a single best fit parameter set was obtained (5 matrix elements), although four further parameter sets were within 1% of the lowest χ^2 obtained and differed in the parallel continuum. In these cases, additional data and/or cross-checks on the determined matrix elements are therefore desirable to confirm their validity. In these cases, all sets of matrix elements determined resulted in satisfactory fits to the time-series data, hence comparison with the data at different rotational revivals was not a sufficiently stringent cross-check.

For the B-channel, the single lowest χ^2 result was selected as the best result, with the proviso that this cannot be determined to be unique. The resulting MF reconstruction was found to bear some resemblance to the *ab initio* results (fig. 2), while the four alternative parameter sets yielded quite different MF reconstructions. In this case, data with better S/N should yield a more definitive result, and reduce the uncertainties on the retrieved phases (table III).

For the A-channel, the best set of perpendicular matrix elements ($q = \pm 1$) were selected post-facto [16–18], by comparison with ePolyScat results, again with the proviso that this requirement may be indicative of a non-unique result set. In this case, the selected matrix elements yield MF results which compare well with the *ab initio* results. It is not expected that better data would be sufficient to obtain a unique result in this case - the issue is rather that the $\beta_{L,M}(t)$ for $L > 0$ are relatively insensitive to the axis distribution (fig. 1(b)), a consequence of the details of the ionization matrix elements (see ref. [3] for general discussion on this issue). In this case, measurements with a different polarization geometry may provide the required additional information, although the Π symmetry may still provide restrictions - see, for instance, ref. [35], wherein limitations imposed by initial and final state symmetries in the related case of matrix element retrieval from MFPADs are discussed.

V. PHOTOIONIZATION MATRIX ELEMENTS

Tables I-III list the unique $\boldsymbol{D}_{hl}^{\Gamma\mu}(q)$ obtained for each photoionization channel. In each case, the retrieved elements are broken down by irreducible representation ($D_{\infty h}$ point group), and relevant indicies. In this case, the h index correlates

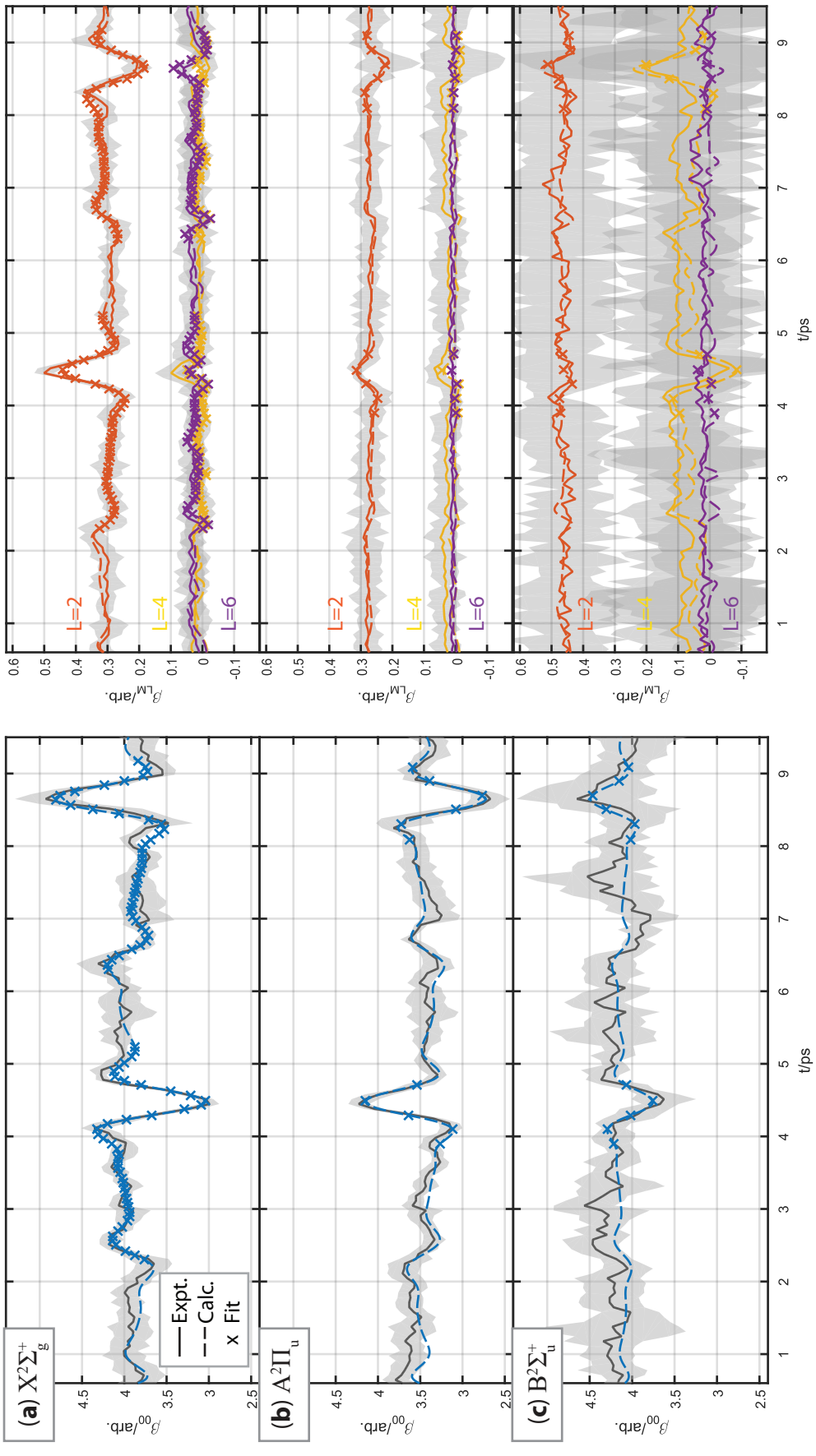

Figure 1. Retrieval of the ionization matrix elements from the time-series data. Left column shows the calculation results from eqn. 2 for the X, A and B-channel yields, $\beta_{00}(t)$ (as per fig. 3 in the main text), right column shows the $\beta_{L,M}(t)$ for $L = 2, 4, 6$, $M = 0$ for each case; 'x' marks points included in the fit and the grey envelopes indicate the experimental uncertainties, derived as the standard-deviation of repeat measurements.

with $\pm m$ states, and μ with degenerate components of the ionizing orbital. In all cases with $q = \pm 1$, the sign of the contributing m terms are correlated or anti-correlated as indicated in the tables. In degenerate cases the full set of symmetrized matrix elements for $D_{\infty h}$ require additional elements, which are essentially transformations derived from the minimal unique values listed here; these are also given where required. In all cases the lowest-order phase is chosen as the reference phase (since absolute values cannot be obtained), and set to zero.

As discussed above, for the X and B-channels, unique sets of matrix elements were obtained, although other sets within 1% of the best results were also obtained for the B-channel, suggesting the possibility of multiple solutions at the coarse level of fitting employed. For the A-channel, two parameter sets were obtained, and the results shown here correspond to the set which provided the MFPADs which most closely matched the *ab initio* MFPADs (i.e. selected by post-hoc verification and corroboration). These matrix elements correspond to the results provided in the main article.

The matrix elements are normalized such that the sum of the squares over each continuum is unity, and phases are defined on the interval $-\pi \geq \arg(\boldsymbol{D}_{hl}^{\Gamma\mu}(q)) \geq \pi$ (note that absolute signs are not defined in this case, hence switching the sign of all phases produces the same PADs - see discussion in Sect. II above for details). Uncertainties in the parameters are given in parentheses; these values were determined via curvature of the χ^2 hyperspace along each dimension [36], an extended discussion on this topic may be found in [33]. For the X-state, with the highest quality experimental data, the results are generally good, with relatively small uncertainties for all parameters except for the phase of the f-wave ($l = 3$) for $m = \pm 1$. In this, and similar cases (indicated in *italics* in tables I-III) this analysis indicated large uncertainties, suggesting that the associated values are not well-defined by the data, although it is also of note that this analysis treats each dimension independently and may lead to spurious results in certain cases [33]. For the B-state, where the experimental data is noisy, this is expected. For the A-state, there is little dependence of $\beta_{LM}(t)$ on the alignment observed for $L > 0$, and this has resulted in large uncertainties in the phases, although the magnitudes are well-defined; in this case, the ionization dynamics - which involves a relatively isotropic π_u ionizing orbital, with (x, y) orientation undefined in the LF - may restrict the fidelity of the reconstruction for the $q = \pm 1$ case. Final-state averaging over the larger energy-span of the band (relative to the X and B bands) may also contribute to the larger uncertainties here. More work is required here to ascertain whether this is a fundamental limitation for this specific case, and whether this could be alleviated by additional data (e.g. different align-pump polarization geometry) which provides distinct interferences, thus additional phase sensitivity, in the observable AFPADs.

Despite these issues in some cases, the comparison of the MFPADs with *ab initio* results validates the matrix elements retrieved to some degree and suggests that the details, such as a significant $l = 5$ contribution for the X-channel, are generally robust. Physically, the scattering dynamics is complicated, due to both the two-centre scatterer, and the shape of the initial molecular orbital. In both cases, multiple l-waves are required, and atomic-like selection rules ($\Delta l = \pm 1$) cannot be applied to the ionization event. For general discussion on these points in molecular photoionization see, for example, refs. [8, 14, 37] and refs. therein; for N_2 scattering specifically, see ref. [17] and ref. [27] for an investigation of vibrational (bond-length) effects. Finally, it is of note that the axis distribution was found to contain significant terms to $K_{max} = 6$ (see online data repository), but these terms were generally small. Since this will mitigate the contribution of higher l terms to the observable (via the limit $L \leq P + K$, as discussed above, hence l due to the limit $L \leq l + l'$), the results may be under-defined for the $l = 5$ term, although this is not confirmed by our uncertainty analysis (which gives relatively small uncertainties here).

Γ	q	h	μ	l	m	$\lvert\boldsymbol{D}_{hl}^{\Gamma\mu}(q)\rvert$	$\arg(\boldsymbol{D}_{hl}^{\Gamma\mu}(q))$	$b_{hl\lambda}^{\Gamma\mu}$	Relations
σ_u	0	1	1	1	0	0.53(2)	0*	1	-
				3	0	0.41(2)	1.1(1)	1	-
				5	0	0.49(2)	1.3(4)	1	-
π_u	± 1	1	1	1	± 1	0.19(3)	-1.4(1)	$1/\sqrt{2}$	$q: \boldsymbol{D}_{hl}^{\pi_u\mu}(+1) = \boldsymbol{D}_{hl}^{\pi_u\mu}(-1)$
				3	± 1	0.17(3)	*0(1)*	$1/\sqrt{2}$	
				5	± 1	0.30(2)	-1.6(9)	$1/\sqrt{2}$	

Table I. Symmetrized matrix elements, $X^2\Sigma_g^+$. The sum over all moduli squared are normalized to unity, $\sum |\boldsymbol{D}_{hl}^{\Gamma\mu}(q)/b_{hl\lambda}^{\Gamma\mu}|^2 = 1$. * reference phase, set to zero. Values in parentheses indicate the uncertainty in the final digit.

Γ	q	h	μ	l	m	$\lvert\boldsymbol{D}_{hl}^{\Gamma\mu}(q)\rvert$	$\arg(\boldsymbol{D}_{hl}^{\Gamma\mu}(q))$	$b_{hl\lambda}^{\Gamma\mu}$	Relations
σ_g	±1	1	1,2	0	0	0.58(3)	0*	$1/\sqrt{2}$	$q(\mu=1):\ \boldsymbol{D}_{hl}^{{\sigma_g}^1}(+1)=\boldsymbol{D}_{hl}^{{\sigma_g}^1}(-1)$
									$q(\mu=2):\ \boldsymbol{D}_{hl}^{{\sigma_g}^2}(+1)=-\boldsymbol{D}_{hl}^{{\sigma_g}^2}(-1)$
									$\mu:\ \boldsymbol{D}_{hl}^{{\sigma_g}^2}(+1)=\Im[\boldsymbol{D}_{hl}^{{\sigma_g}^1}(+1)]-i\Re[\boldsymbol{D}_{hl}^{{\sigma_g}^1}(+1)]$
				2	0	0.23(6)	*0.3(12)*	$1/\sqrt{2}$	
				4	0	0.15(7)	*-0.5(9)*	$1/\sqrt{2}$	
δ_g	±1	1	1,2	2	∓2	0.15(7)	-0.5(2)	$1/\sqrt{2}$	$q(\mu=1):\ \boldsymbol{D}_{hl}^{{\delta_g}^1}(+1)=\boldsymbol{D}_{hl}^{{\delta_g}^1}(-1)$
									$q(\mu=2):\ \boldsymbol{D}_{hl}^{{\delta_g}^2}(+1)=-\boldsymbol{D}_{hl}^{{\delta_g}^2}(-1)$
									$\mu:\ \boldsymbol{D}_{hl}^{{\delta_g}^2}(+1)=-\Im[\boldsymbol{D}_{hl}^{{\delta_g}^1}(+1)]+i\Re[\boldsymbol{D}_{hl}^{{\delta_g}^1}(+1)]$
				4	∓2	0.22(6)	*-0.6(8)*	$1/\sqrt{2}$	
π_g	0	1,2	1,2	2	±1	0.15(5)	*-0.3(30)*	$1/\sqrt{2}$	$h(\mu=1):\ \boldsymbol{D}_{1l}^{{\pi_g}^1}(0)=\boldsymbol{D}_{2l}^{{\pi_g}^1}(0)$
									$h(\mu=2):\ \boldsymbol{D}_{1l}^{{\pi_g}^2}(0)=-\boldsymbol{D}_{2l}^{{\pi_g}^2}(0)$
									$\mu:\ \boldsymbol{D}_{hl}^{{\pi_g}^2}(0)=\Im[\boldsymbol{D}_{hl}^{{\pi_g}^1}(0)]-i\Re[\boldsymbol{D}_{hl}^{{\delta_g}^1}(0)]$
				4	±1	*0.05(9)*	*0.6(30)*	$1/\sqrt{2}$	

Table II. Symmetrized matrix elements, $A^2\Pi_u$. The sum over all moduli squared are normalized to unity, $\sum|\boldsymbol{D}_{hl}^{\Gamma\mu}(q)/b_{hl\lambda}^{\Gamma\mu}|^2=1$. * reference phase, set to zero. Values in parentheses indicate the uncertainty in the final digit.

Γ	q	h	μ	l	m	$\lvert\boldsymbol{D}_{hl}^{\Gamma\mu}(q)\rvert$	$\arg(\boldsymbol{D}_{hl}^{\Gamma\mu}(q))$	$b_{hl\lambda}^{\Gamma\mu}$	Relations
σ_g	0	1	1	0	0	*0.08(21)*	0*	1	-
				2	0	0.19(9)	*-1.0(13)*	1	-
				4	0	0.65(4)	*-1.6(19)*	1	-
π_g	±1	1	1	2	∓1	*0.01(12)*	*-3.5(35)*	$1/\sqrt{2}$	$q:\ \boldsymbol{D}_{hl}^{\pi_u\mu}(+1)=\boldsymbol{D}_{hl}^{\pi_u\mu}(-1)$
				4	∓1	0.52(3)	*0.4(13)*		

Table III. Symmetrized matrix elements, $B^2\Sigma_u^+$. The sum over all moduli squared are normalized to unity, $\sum|\boldsymbol{D}_{hl}^{\Gamma\mu}(q)/b_{hl\lambda}^{\Gamma\mu}|^2=1$. * reference phase, set to zero. Values in parentheses indicate the uncertainty in the final digit.

VI. MOLECULAR FRAME RECONSTRUCTIONS

Figure 2 provides the full set of MF reconstructions, extending fig. 4 in the main manuscript. The reconstructed MFPADs are obtained from eqn. 4, and the matrix elements obtained from the experimental data, as given in tables I-III. The calculated MFPADs were obtained using ePolyScat [38, 39] to compute the ionization matrix elements, and ePSproc for post-processing [40, 41]; full data can be obtained from the online repository. Note that, due to differences in definitions, the ePolyScat matrix elements therein should not be compared directly to those defined by eqn. 4, although the MFPADs obtained independently via the two different formalisms can be compared directly.

As noted in the main text, "the consistency between the ab initio and experimental reconstructions can be taken as a good indicator that both methodologies are robust." However, any differences are, of course, also of interest. In particular, the difference in the lobes at close to 45° in the experiment reconstructions for the X-channel (fig. 2(a)), which are more pronounced in the experimental reconstructions for both continua, does suggest some difference in the higher-order terms obtained from experiment and the theoretical results. These correlate with terms $L>2$, so contain contributions from both $l=3$ and $l=5$ partial waves.

Physically, the scattering dynamics is complicated, due to both the two-centre scatterer, and the shape of the initial molecular orbital. In both cases, multiple l-waves are required to describe the core region where the potential is non-centrally-symmetric, and (l,m) states are mixed (i.e. l and m are not a good quantum numbers). Consequently, atomic-like selection rules ($\Delta l=\pm1$) cannot be applied and the scattering of the outgoing wave is, by definition, multi-polar. Generally, for molecular scatterers, one expects a large range of l-waves to be present, although the details are scatterer and energy specific; however, even in complex cases, lower l terms are expected to dominate, primarily due to the small overlap between higher l bound and continuum components. In this case, it is of note that large high l terms are observed for the X and B-channels, while smaller l are more significant for the A-channel. This observation is broadly consistent with the forms of the ionizing molecular orbitals and the observed time-dependence - for the A-channel the doubly-degenerate Π orbital, and subsequent AF photoionization dynamics, there is lower overall anisotropy than the more 'directional' Σ states.

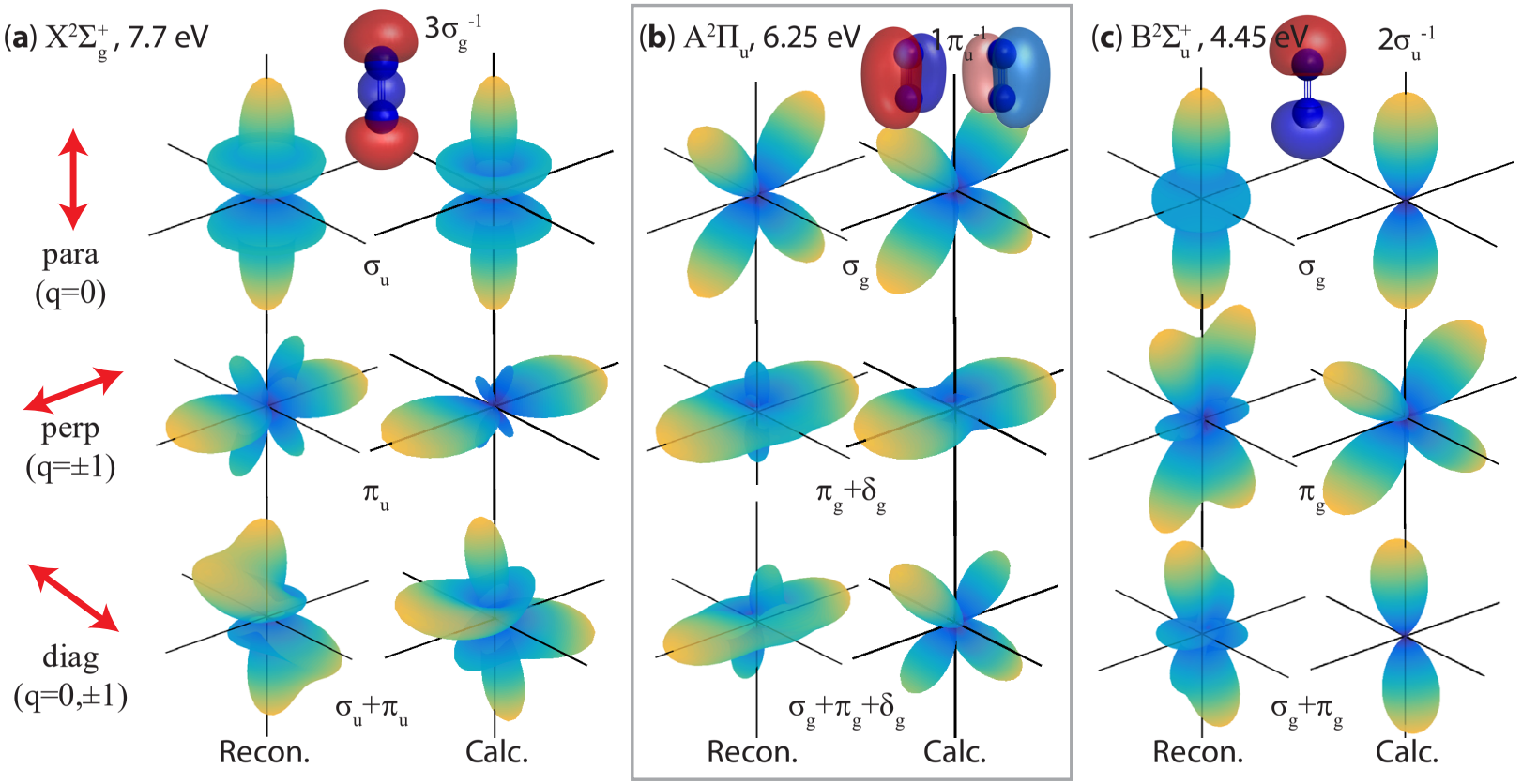

Figure 2. Molecular frame reconstruction as a function of ionizing orbital and polarization geometry. (Recon) MFPADs reconstructed from the experimental analysis; (Calc.) determined from ab initio calculations. Each panel also shows the ionizing orbital, and labels indicate the MF polarization geometry (photon projection q) and corresponding symmetries for the ionization continua accessed.

However, the fact that the differences between the *ab initio* and experimental MFPADs indicate differences in the higher-l terms suggests further work to investigate the scattering physics in more detail. In particular, experiments with different information content could form part of a 'pre-processing' approach (sec. II) to investigate these higher-l terms, and reduce the phase errors in some cases. For example, the preparation of axis distributions with higher K ($K > 6$) would result in a higher sensitivity to higher l terms in the measurement (see eqn. 2). These types of considerations, in the case of symmetric tops, are discussed in refs. [3, 22], for the most general case of an asymmetric top, work is ongoing [21]. Further *ab initio* work considering the effects of both physical parameters (e.g. bond-length) and computational methods (e.g. level of electronic structure theory) is also underway.

VII. DATA & CODE

As noted above, raw data and processing code is available online at https://dx.doi.org/10.6084/m9.figshare.4480349. This repository is broadly in line with Open Science/TOP guidelines [42], and it is hoped that this provides a foundation for other investigators to explore and build on the methodology presented herein.

This repository contains the following:

- XUV ionization time-series data, experimental data as shown in Fig. 1.
- ADM fitting and extraction, as shown in Fig. 2 of the main article.
- BLM fitting and matrix element extraction, fit results as shown in Fig. 1, and full matrix elements as given in tables I-III.
- ePolyScat calculations, raw results and plots (e.g. as shown in Fig. 2), including dependence on kinetic energy over 1 eV ranges. The raw results can be processed with ePSproc [40, 41].
- Data plotting codes.
- AFPAD code and fitting routines. Note that, although this code is, in principle, suitable for any AFPAD computation, it is currently not generalised to asymmetric top problems, nor compatible with ePolyScat matrix elements due to differences in the definitions employed. Nonetheless, it is included here to provide a complete accounting of the methodology used, and provide a resource for other investigators [43]. In the future, improved versions of this code will be released. As detailed in the main text, work on improved fitting methodologies is in progress, and integration with ePSproc codes [40, 41] is also planned.

The data and plotting codes are currently provided in Matlab/Octave format.

* paul.hockett@nrc.ca

[1] Jonathan G. Underwood and Katharine L. Reid. Time-resolved photoelectron angular distributions as a probe of intramolecular dynamics: Connecting the molecular frame and the laboratory frame. *The Journal of Chemical Physics*, 113(3):1067, 2000. ISSN 00219606. doi:10.1063/1.481918. URL http://link.aip.org/link/JCPSA6/v113/i3/p1067/s1&Agg=doi.

[2] Albert Stolow and Jonathan G. Underwood. Time-Resolved Photoelectron Spectroscopy of Non-Adiabatic Dynamics in Polyatomic Molecules. In Stuart A. Rice, editor, *Advances in Chemical Physics*, volume 139 of *Advances in Chemical Physics*, chapter 6, pages 497–584. John Wiley & Sons, Inc., Hoboken, NJ, USA, March 2008. ISBN 9780470259498. doi:10.1002/9780470259498.ch6. URL http://doi.wiley.com/10.1002/9780470259498.

[3] Paul Hockett. General phenomenology of ionization from aligned molecular ensembles. *New Journal of Physics*, 17(2): 23069, 2015. ISSN 1367-2630. doi:10.1088/1367-2630/17/2/023069. URL http://dx.doi.org/10.1088/1367-2630/17/2/023069.

[4] Dan Dill. Fixed-molecule photoelectron angular distributions. *The Journal of Chemical Physics*, 65(3):1130–1133, 1976. doi:10.1063/1.433187. URL http://link.aip.org/link/?JCP/65/1130/1.

[5] Albert Messiah. *Quantum Mechanics Volume I*. North-Holland Publishing Company, 1970.

[6] N Chandra. Photoelectron spectroscopic studies of polyatomic molecules. i. theory. *Journal of Physics B: Atomic and Molecular Physics*, 20(14):3405–3415, 1987. URL http://stacks.iop.org/0022-3700/20/3405.

[7] Katharine L. Reid, David J. Leahy, and Richard N. Zare. Effect of breaking cylindrical symmetry on photoelectron angular distributions resulting from resonance-enhanced two-photon ionization. *The Journal of Chemical Physics*, 95(3):1746–1756, 1991. doi:10.1063/1.461023. URL http://link.aip.org/link/?JCP/95/1746/1.

[8] Hongkun Park and Richard N. Zare. Molecular-orbital decomposition of the ionization continuum for a diatomic molecule by angle- and energy-resolved photoelectron spectroscopy. i. formalism. *The Journal of Chemical Physics*, 104(12):4554–4567, 1996. doi:10.1063/1.471204. URL http://link.aip.org/link/?JCP/104/4554/1.

[9] Katharine L. Reid and Ivan Powis. Symmetry considerations in molecular photoionization: Fixed molecule photoelectron angular distributions in C3v molecules as observed in photoelectronâphotoion coincidence experiments. *The Journal of Chemical Physics*, 100(2):1066, 1994. ISSN 00219606. doi:10.1063/1.466638. URL http://scitation.aip.org/content/aip/journal/jcp/100/2/10.1063/1.466638.

[10] Robert R. Lucchese, Georges Raseev, and Vincent McKoy. Studies of differential and total photoionization cross sections of molecular nitrogen. *Physical Review A*, 25(5):2572–2587, May 1982. doi:10.1103/PhysRevA.25.2572.

[11] Yasuki Arasaki, Kazuo Takatsuka, Kwanghsi Wang, and Vincent McKoy. Femtosecond energy- and angle-resolved photoelectron spectra. *Chemical Physics Letters*, 302(5-6):363 – 374, 1999. ISSN 0009-2614. doi:DOI: 10.1016/S0009-2614(99)00153-0. URL http://www.sciencedirect.com/science/article/B6TFN-3W4PP41-1/2/4b6b92fcbd2488b366022d2e3d081df2.

[12] David J. Leahy, Katharine L. Reid, and Richard N. Zare. Complete description of two-photon (1+1[script ']) ionization of no deduced from rotationally resolved photoelectron angular distributions. *The Journal of Chemical Physics*, 95(3):1757–1767, 1991. doi:10.1063/1.461024. URL http://link.aip.org/link/?JCP/95/1757/1.

[13] O. Geßner, Y. Hikosaka, B. Zimmermann, A. Hempelmann, R. R. Lucchese, J. H. D. Eland, P.-M. Guyon, and U. Becker. $4\sigma - 1$ inner valence photoionization dynamics of no derived from photoelectron-photoion angular correlations. *Physical Review Letters*, 88(19):193002, Apr 2002. doi:10.1103/PhysRevLett.88.193002.

[14] Paul Hockett, Michael Staniforth, Katharine L. Reid, and Dave Townsend. Rotationally resolved photoelectron angular distributions from a nonlinear polyatomic molecule. *Physical Review Letters*, 102(25):253002, Jun 2009. doi:10.1103/PhysRevLett.102.253002.

[15] Katharine Reid, David Leahy, and Richard Zare. Complete description of molecular photoionization from circular dichroism of rotationally resolved photoelectron angular distributions. *Physical Review Letters*, 68(24):3527–3530, jun 1992. ISSN 0031-9007. doi:10.1103/PhysRevLett.68.3527. URL http://link.aps.org/doi/10.1103/PhysRevLett.68.3527.

[16] Yoshi-Ichi Suzuki, Ying Tang, and Toshinori Suzuki. Time-energy mapping of photoelectron angular distribution: application to photoionization stereodynamics of nitric oxide. *Physical chemistry chemical physics : PCCP*, 14(20):7309–20, May 2012. ISSN 1463-9084. doi:10.1039/c2cp40308k. URL http://pubs.rsc.org/en/content/articlehtml/2012/cp/c2cp40308k.

[17] Akira Yagishita, Kouichi Hosaka, and Jun-Ichi Adachi. Photoelectron angular distributions from fixed-in-space molecules. *Journal of Electron Spectroscopy and Related Phenomena*, 142(3):295 – 312, 2005. ISSN 0368-2048. doi:DOI: 10.1016/j.elspec.2004.09.005. URL http://www.sciencedirect.com/science/article/B6TGC-4DVW2XM-1/2/4200b83f67d15b8c407326659aed6d1d. Modern Electron Spectroscopy of Atoms and Molecules. A collection of invited papers dedicated to Professor Katsumi Kimura in recognition of an esteemed research career spanning a 50-year period.

[18] Ying Tang, Yoshi-Ichi Suzuki, Takuya Horio, and Toshinori Suzuki. Molecular Frame Image Restoration and Partial Wave Analysis of Photoionization Dynamics of NO by Time-Energy Mapping of Photoelectron Angular Distribution. *Physical Review Letters*, 104(7):073002, February 2010. ISSN 0031-9007. doi:10.1103/PhysRevLett.104.073002. URL http://link.aps.org/doi/10.1103/PhysRevLett.104.073002.

[19] Yi-Yian Yin, Ce Chen, D. S. Elliott, and A. V. Smith. Asymmetric photoelectron angular distributions from interfering photoionization processes. *Physical Review Letters*, 69(16):2353–2356, Oct 1992. doi:10.1103/PhysRevLett.69.2353.

[20] Yi-Yian Yin, D. S. Elliott, R. Shehadeh, and E. R. Grant. Two-pathway coherent control of photoelectron angular distributions in molecular no. *Chemical Physics Letters*, 241(5-6):591 – 596, 1995. ISSN 0009-2614. doi:DOI: 10.1016/0009-2614(95)00647-M. URL http://www.sciencedirect.com/science/article/B6TFN-3YCN3B1-BR/2/9cf94c712099f5fa63e68636678babed.

[21] Varun Makhija and Paul Hockett. General Phenomenology of Ionization from Aligned Molecular Ensembles II: Asymmetric tops & extraction of matrix elements. *In Preparation*, 2017.

[22] S Ramakrishna and Tamar Seideman. On the information content of time- and angle-resolved photoelectron spectroscopy. *Journal of Physics B: Atomic, Molecular and Optical Physics*, 45(19):194012, October 2012. ISSN 0953-4075. doi:10.1088/0953-4075/45/19/194012. URL http://stacks.iop.org/0953-4075/45/i=19/a=194012?key=crossref.68faa78abc832ed11020afde085ac486.

[23] S. Ramakrishna and Tamar Seideman. Rotational wave-packet imaging of molecules. *Physical Review A*, 87(2):023411, February 2013. ISSN 1050-2947. doi:10.1103/PhysRevA.87.023411. URL http://link.aps.org/doi/10.1103/PhysRevA.87.023411.

[24] Tamar Seideman and Stuart C. Althorpe. Time-resolved photoelectron angular distributions as a map of rotational motion. *Journal of Electron Spectroscopy and Related Phenomena*, 108(1-3):99–108, July 2000. ISSN 03682048. doi:10.1016/S0368-2048(00)00131-6. URL http://linkinghub.elsevier.com/retrieve/pii/S0368204800001316.

[25] Tamar Seideman. Time-resolved photoelectron angular distributions as a probe of coupled polyatomic dynamics. *Physical Review A*, 64(4):042504, Sep 2001. doi:10.1103/PhysRevA.64.042504.

[26] Tamar Seideman. Time-resolved photoelectron angular distributions: Concepts, applications, and directions. *Annual Review of Physical Chemistry*, 53(1):41–65, 2002.

[27] J.A. López-Domínguez, David Hardy, Aloke Das, E.D. Poliakoff, Alex Aguilar, and Robert R. Lucchese. Mechanisms of Franck-Condon breakdown over a broad energy range in the valence photoionization of N2 and CO. *Journal of Electron Spectroscopy and Related Phenomena*, 185(8-9):211–218, sep 2012. ISSN 03682048. doi:10.1016/j.elspec.2012.06.016. URL http://linkinghub.elsevier.com/retrieve/pii/S0368204812000710.

[28] Ping Lin and Robert R. Lucchese. Total cross sections and molecular frame photoelectron angular distributions in the Nâ1s photoionization of N[sub 2]: An investigation of electron correlation effects. *The Journal of Chemical Physics*, 117(9):4348, 2002. ISSN 00219606. doi:10.1063/1.1488576. URL http://link.aip.org/link/JCPSA6/v117/i9/p4348/s1{&}Agg=doi.

[29] Andreas Osterwalder, Matthew J. Nee, Jia Zhou, and Daniel M. Neumark. High resolution photodetachment spectroscopy of negative ions via slow photoelectron imaging. *Journal of Chemical Physics*, 121(13):6317–6322, 2004. ISSN 00219606.

doi:10.1063/1.1787491.

[30] Paul Hockett. *Photoionization dynamics of polyatomic molecules*. PhD thesis, University of Nottingham, 2009. URL http://eprints.nottingham.ac.uk/10857/.

[31] Paul Hockett, Christer Z. Bisgaard, Owen J. Clarkin, and Albert Stolow. Time-resolved imaging of purely valence-electron dynamics during a chemical reaction. *Nature Physics*, 7(8):612–615, apr 2011. ISSN 1745-2473. doi:10.1038/nphys1980. URL http://www.nature.com/doifinder/10.1038/nphys1980.

[32] Paul Hockett. Quantum Dynamical Imaging via Time-resolved Photoelectron Interferometry: Beyond a Phenomenological Imaging of Molecular Dynamics, DOI: 10.6084/m9.figshare.3580734, 2014. URL https://doi.org/10.6084/m9.figshare.3580734.

[33] Paul Hockett, Matthias Wollenhaupt, Christian Lux, and Thomas Baumert. Complete photoionization experiments via ultrafast coherent control with polarization multiplexing. II. Numerics and analysis methodologies. *Physical Review A*, 92(1):013411, jul 2015. ISSN 1050-2947. doi:10.1103/PhysRevA.92.013411. URL http://link.aps.org/doi/10.1103/PhysRevA.92.013411.

[34] Varun Makhija, Xiaoming Ren, Drue Gockel, Ahn-Thu Le, and Vinod Kumarappan. Orientation Resolution through Rotational Coherence Spectroscopy. pages 1–6, 2016. URL http://arxiv.org/abs/1611.06476.

[35] R. R. Lucchese, A. Lafosse, J. C. Brenot, P. M. Guyon, J. C. Houver, M. Lebech, G. Raseev, and D. Dowek. Polar and azimuthal dependence of the molecular frame photoelectron angular distributions of spatially oriented linear molecules. *Physical Review A*, 65(2):020702, Jan 2002. doi:10.1103/PhysRevA.65.020702.

[36] Philip R. Bevington and D. Keith Robinson. *Data Reduction and Error Analysis for the Physical Sciences*. McGraw-Hill, New York, 2nd edition, 1992.

[37] Katharine L. Reid. Photoelectron angular distributions. *Annual Review of Physical Chemistry*, 54(1):397–424, 2003. doi:10.1146/annurev.physchem.54.011002.103814. URL http://arjournals.annualreviews.org/doi/abs/10.1146/annurev.physchem.54.011002.103814.

[38] F. A. Gianturco, R. R. Lucchese, and N. Sanna. Calculation of low-energy elastic cross sections for electron-CF4 scattering. *The Journal of Chemical Physics*, 100(9):6464, may 1994. ISSN 00219606. doi:10.1063/1.467237. URL http://scitation.aip.org/content/aip/journal/jcp/100/9/10.1063/1.467237.

[39] Alexandra P P Natalense and Robert R Lucchese. Cross section and asymmetry parameter calculation for sulfur 1s photoionization of SF[sub 6]. *The Journal of Chemical Physics*, 111(12):5344, 1999. ISSN 00219606. doi:10.1063/1.479794. URL http://link.aip.org/link/JCPSA6/v111/i12/p5344/s1{&}Agg=doi.

[40] Paul Hockett. ePSproc: Post-processing for ePolyScat (v1.0.0), 2016. URL https://figshare.com/articles/ePSproc{_}Post-processing{_}for{_}ePolyScat{_}v1{_}0{_}0{_}/3545639.

[41] Paul Hockett. ePSproc: Post-processing suite for ePolyScat electron-molecule scattering calculations. *Authorea*, 2016. doi:10.6084/m9.figshare.3545639. URL http://dx.doi.org/10.6084/m9.figshare.3545639.

[42] B. A. Nosek, G. Alter, G. C. Banks, D. Borsboom, S. D. Bowman, S. J. Breckler, S. Buck, C. D. Chambers, G. Chin, G. Christensen, M. Contestabile, A. Dafoe, E. Eich, J. Freese, R. Glennerster, D. Goroff, D. P. Green, B. Hesse, M. Humphreys, J. Ishiyama, D. Karlan, A. Kraut, A. Lupia, P. Mabry, T. Madon, N. Malhotra, E. Mayo-Wilson, M. McNutt, E. Miguel, E. Levy Paluck, U. Simonsohn, C. Soderberg, B. A. Spellman, J. Turitto, G. VandenBos, S. Vazire, E. J. Wagenmakers, R. Wilson, and T. Yarkoni. Promoting an open research culture. *Science*, 348(6242):1422–1425, jun 2015. ISSN 0036-8075. doi:10.1126/science.aab2374. URL http://science.sciencemag.org.proxy.bib.uottawa.ca/content/348/6242/1422.fullhttp://www.sciencemag.org/cgi/doi/10.1126/science.aab2374.

[43] Nick Barnes. Publish your computer code: it is good enough. *Nature*, 467(7317):753, oct 2010. ISSN 1476-4687. doi:10.1038/467753a. URL http://www.nature.com/news/2010/101013/full/467753a.html.